Calculations of the polarization spectrum by two-photon absorption in the hydrogen Lyman-α line

Marco Antonio Gigosos*
Departamento de Óptica, Universidad de Valladolid, 47071 Valladolid, Spain

Manuel Ángel González
Departamento de Termodinámica, Universidad de Valladolid, 47071 Valladolid, Spain

(Received 23 December 1997; revised manuscript received 18 May 1998)

We present calculations, obtained by computer simulation, of the polarization spectrum by two-photon absorption in the transition $1S \rightarrow 2S$ of hydrogen in plasmas at low electronic density. Fine structure and ion dynamic effects have been included. The obtained results allow one to make a map of linewidths as a function of the electronic density and temperature to be applied for diagnosis in plasmas. [S1063-651X(98)08710-8]

PACS number(s): 52.65.−y, 32.60.+i, 32.70.Jz

I. INTRODUCTION

The computer simulation methods applied to the calculation of Stark broadened spectral line shapes have been shown to be the most accurate [1] in spite of the volume of necessary calculation. These methods have been used since the 1980s, on one hand to study isolated phenomena as if they were an ideal laboratory [2–4], and on the other hand to make tables of practical use in diagnosis of plasmas [5,6]. In this work we present a calculation done by computer simulation of the spectrum of the Stark broadened Lyman-α transition of the hydrogen that is obtained when one uses polarization spectroscopy by two-photon absorption techniques. This technique was used for the first time in absorption measurements, that is to say, in processes that only detect the imaginary part of the two-photon susceptibility, in molecular vapors and particularly in the studied transition in this work [7]. In 1976 the polarization spectroscopy by two-photon absorption was employed for the first time, including the detection of the real part of the susceptibility in the $3S \rightarrow 5S$ two-photon transition in sodium vapor [8].

Recently, this spectroscopic method has been applied to the study of the hydrogen $1S \rightarrow 2S$ transition in plasmas (see Refs. [9–14] to which we will refer frequently). The final aim of this work is to provide data on the form of the spectral lines, and especially of their full width at half maximum (FWHM), for doing diagnosis in plasmas in a wide range of electronic densities and temperatures. We will devote special attention to the comparison with the only experimental results that we know of polarization by two-photon absorption spectrum in the studied line.

II. POLARIZATION SPECTROSCOPY

The polarization spectroscopy is based on the measurement of the change of the polarization state of a test wave when it crosses a medium in study. Such a change is induced by a polarized pumping wave. This pumping wave alters the optical behavior of the medium modifying its refraction index and absorption coefficient in a nonisotropic way. In some way, polarization spectroscopy is similar to saturation spectroscopy, that is based on the measure of the absorption of a probe beam in a medium whose optical response is altered by a pumping beam.

The basic idea of the polarization spectroscopy may be well understood analyzing the experimental scheme represented in Fig. 7.20 of Ref. [15] (in this book a very good description of this spectroscopic technique can be found). The laser beam is split into two signals, one of them, the pumping beam, of great intensity, and the other, the probe beam, of weak intensity. The pumping beam passes through a $\lambda/4$ plate in order to be circularly polarized and it is sent to the studied sample. On the other hand, the probe beam crosses a polarizer P_1 that puts the radiation on a linear polarization state. An analyzer P_2 crossed with P_1 is set after the sample and before the detector. When the pumping beam is not present at the medium, the probe beam meets an isotropic medium and the detector only detects certain residual radiation that should be null if both polarizers were perfect. On the contrary, if the pumping beam is present, this induces an optical anisotropy in the medium, that gives rise to an elliptical polarization of the probe wave and, consequently, a certain signal is obtained in the detector [15].

In the experiment that we study in this work [12,14], the probe beam detects the susceptibility induced by a two-photon transition [8,9] between the levels $n=1$ and $n=2$ of the hydrogen atom (Lyman-α). The laser used emits a radiation of 243 nm. The pumping beam produces a transition between the state $1S$ and a virtual state $l=1$, $m=1$ (state p) because it is a circularly polarized σ^+ beam. This fact gives rise to a different saturation of the three possible states of that virtual level: only the state with $m=1$ is saturated. This is equivalent to an anisotropy in the medium because a uniform population of the different m sublevels is not found. In the same process, the probe beam is absorbed, giving rise to the transition between the virtual level and the $n=2$ level. The selection rule $|\Delta l|=1$ imposes the arrival level to be the $2S$ because there is no level with $l=2$ in that range of energies. In that case only the transition with $\Delta m=-1$ is allowed, that is to say, it must absorb the σ^- part of a photon

*Electronic address: gigosos@coyanza.opt.cie.uva.es

of the probe beam. Of course, a process in which the first absorbed photon belongs to the probe beam is possible. In this case only when the transition $1S \rightarrow [m=-1]$ is produced is it possible to reach the upper level $2S$ through a second σ^+ photon of the pumping beam. In either case, this scheme allows us to see that a two-photon transition between the state $n=1$ and $n=2$ is impossible if both photons belong to the pumping beam, because, in that case, it would have to be $|\Delta m|=2$ (see Ref. [10] for a detailed analysis of this experiment).

Modifying the frequency of the laser radiation, the spectrum of the $1S \rightarrow 2S$ transition is covered. In our case, this spectrum is determined by the Stark broadening due to the collisions suffered by the emitter with the charged particles that surround it.

III. SPECTRAL LINE SHAPES

A. Emission spectrum

As is well known, the profile of a spectral line of dipole emission can be obtained from the Fourier transform of the average {} of the autocorrelation function $C(t)$ of the atomic dipole moment $\mathbf{D}(t)$ performed over an ensemble [16]:

$$I(\omega)=\frac{1}{\pi}\,\mathrm{Re}\int_0^\infty dt\{C(t)\}e^{i\omega t}, \tag{1}$$

$$C(t)=\mathrm{tr}[\mathbf{D}(t)\cdot\mathbf{D}(0)], \tag{2}$$

$$\mathbf{D}(t)=U^\dagger(t)\mathbf{D}U(t), \tag{3}$$

where $U(t)$ is the evolution operator of the emitter atom that satisfies the Schrödinger equation

$$i\hbar\frac{d}{dt}U(t)=H(t)U(t)=[H_0+q\mathbf{E}(t)\cdot\mathbf{R}]U(t) \tag{4}$$

in which the Hamiltonian $H(t)$ includes both the structure of the undisturbed states, H_0, and the effects of the charged perturbers on the emitter through the dipole interaction $q\mathbf{E}\cdot\mathbf{R}$. $\mathbf{E}(t)$ is the temporary sequence of the electric microfield.

In most cases, the energy gap between the group of upper levels and the group of lower levels of the transition studied is in the optical or in the ultraviolet range. The collision processes between the emitter and the perturbers give rise to energy exchanges deep under that separation, so that we can assume that they cannot induce transitions between these two groups of states (*no-quenching* approximation). As a consequence, the evolution operator that we will consider has the form

$$U(t)=\begin{pmatrix} U_u(t) & 0 \\ 0 & U_l(t)\end{pmatrix}, \tag{5}$$

where $U_u(t)$ and $U_l(t)$ are two matrices that give the temporary evolution of the states of the upper and lower groups independently.

On the other hand, when considering the emission spectrum, we are only interested in a limited range of frequencies from the center of the spectral line, so that our displacement in frequency is small enough and we do not have to consider dipole transitions beyond those two groups, and much less between the elements of the same group, whose distance in energies is much smaller than that of the corresponding optical transition. In this way, the matrix of the dipole moment has the form

$$\mathbf{D}=\begin{pmatrix} 0 & \mathbf{d} \\ \mathbf{d}^\dagger & 0\end{pmatrix}. \tag{6}$$

So, the trace that appears in Eq. (2) is expressed as

$$C(t)=\mathrm{tr}(U_u^\dagger\mathbf{d}U_l\cdot\mathbf{d}^\dagger)+\mathrm{tr}(U_l^\dagger\mathbf{d}^\dagger U_u\cdot\mathbf{d}). \tag{7}$$

The matrices U_u and U_l are, respectively, the solutions of the equations

$$i\hbar\frac{d}{dt}U_u=H_uU_u, \quad i\hbar\frac{d}{dt}U_l=H_lU_l, \tag{8}$$

with

$$\begin{aligned} H_u&=\mathcal{E}_u+H_{0u}+\mathbf{E}(t)\cdot\mathbf{R}_u, \\ H_l&=\mathcal{E}_l+H_{0l}+\mathbf{E}(t)\cdot\mathbf{R}_l, \end{aligned} \tag{9}$$

where $\mathcal{E}_u+H_{0u}$ and $\mathcal{E}_l+H_{0l}$ are the projections of the complete Hamiltonian of the unperturbed emitter on the subspaces of the upper and lower states, respectively, and similarly with the projections of the $\mathbf{R}$ operator on those same subspaces. The matrices $\mathcal{E}_u$ and $\mathcal{E}_l$, that are proportional to the unit matrix, give the separation in energies between the two groups of states. We can omit these constant quantities putting in Eq. (7) $U_u\exp(-i\mathcal{E}_ut/\hbar)$ and $U_l\exp(-i\mathcal{E}_lt/\hbar)$ instead of U_u and U_l, respectively, so that we can write the autocorrelation function in the form

$$C(t)=e^{i\omega_0t/\hbar}\,\mathrm{tr}(U_u^\dagger\mathbf{d}U_l\cdot\mathbf{d}^\dagger)+e^{-i\omega_0t/\hbar}\,\mathrm{tr}(U_l^\dagger\mathbf{d}^\dagger U_u\cdot\mathbf{d}), \tag{10}$$

with $\omega_0\equiv(\mathcal{E}_u-\mathcal{E}_l)/\hbar$. If we set

$$\mathrm{tr}(U_l^\dagger\mathbf{d}^\dagger U_u\cdot\mathbf{d})\equiv C_R(t)+iC_I(t), \tag{11}$$

where $C_R(t)$ and $C_I(t)$ are real functions of the time, then,

$$C(t)=2C_R(t)\cos(\omega_0t)+2C_I(t)\sin(\omega_0t), \tag{12}$$

and, the emission profile is

$$\begin{aligned} I(\omega)&=\frac{1}{\pi}\int_0^\infty dt\,\cos(\omega t)[2C_R(t)\cos(\omega_0t) \\ &\quad+2C_I(t)\sin(\omega_0t)] \\ &=\frac{1}{\pi}\int_0^\infty dt(\{\cos[(\omega+\omega_0)t]+\cos[(\omega-\omega_0)t]\}C_R(t) \\ &\quad+\{\sin[(\omega+\omega_0)t]-\sin[(\omega-\omega_0)t]\}C_I(t)). \end{aligned} \tag{13}$$

We set $\omega=\omega_0+\Delta\omega$, and we calculate the spectrum around the frequency ω_0. Furthermore, we will not take into account the contribution to the spectrum of quantities as

$\int_0^\infty dt\ \cos[(\omega+\omega_0)t]C_R(t)$ that would only make sense if the function $C_R(t)$ or $C_I(t)$ had variations in time in that scale of frequencies. Then we have

$$I(\Delta\omega)=\frac{1}{\pi}\int_0^\infty dt[\cos(\Delta\omega t)C_R(t)-\sin(\Delta\omega t)C_I(t)]. \tag{14}$$

B. Absorption spectrum

We are interested in calculating the absorption profile in a very narrow gap around the central frequency ω_0. So, the shapes of the emission and absorption profiles are the same [17–19]. From now on, we will talk indistinctly about the emission or the absorption profile.

C. Dispersion spectrum

The form of the polarization profile is the sum of the squares of the absorption and the dispersion profiles (see page 456 of [15]) that are related to each other through the Kramers–Kronig equations. Thus, if $A(x)$ is the absorption profile, the dispersion profile is [20]

$$D(x)=\frac{1}{\pi}\,\mathrm{P}\int_{-\infty}^{+\infty}\frac{A(y)}{y-x}dy, \tag{15}$$

where P denotes principal value.

The absorption profile is given by Eq. (1). In order to obtain the principal value of the expression (15) we set

$$\frac{A(y)}{y-x}=\frac{A(x)}{y-x}+\frac{A(y)-A(x)}{y-x}. \tag{16}$$

We will suppose that $A(x)$ is derivable, so that the principal value of the second term of the member on the right of Eq. (16) coincides with the ordinary integral [in the limit $y\to x$ the integrand tends to $dA(x)/dx$]. On the other hand, the first term of the member on the right of Eq. (16) is a function of y antisymmetric with respect to the point x, so that $\mathrm{P}\int_{-\infty}^{+\infty}A(x)dy/(y-x)=0$. Therefore [21]

$$D(x)=\frac{1}{\pi}\int_{-\infty}^{+\infty}\frac{A(y)-A(x)}{y-x}dy. \tag{17}$$

Taking into account the form of the absorption profile,

$$\frac{A(y)-A(x)}{y-x}=\frac{1}{\pi}\,\mathrm{Re}\int_0^\infty\frac{e^{iyt}-e^{ixt}}{y-x}C(t)dt$$

$$=\frac{1}{\pi}\,\mathrm{Re}\int_0^\infty ie^{ixt}\frac{\sin\left(\frac{y-x}{2}t\right)}{\frac{y-x}{2}}e^{i[(y-x)/2]t}C(t)dt. \tag{18}$$

Thereby,

$$D(x)=\frac{2}{\pi^2}\,\mathrm{Re}\int_0^\infty ie^{ixt}C(t)dt\int_{-\infty}^{+\infty}dz\,\frac{\sin z}{z}e^{iz}, \tag{19}$$

where we have introduced the variable change $z=(y-x)t/2$ in the last integral. Since $\int_{-\infty}^{+\infty}e^{iz}\,\sin(z)/z=\pi/2$, we finally obtain

$$D(\omega)=\frac{1}{\pi}\,\mathrm{Re}\int_0^\infty iC(t)dte^{i\omega t}=-\frac{1}{\pi}\,\mathrm{Im}\int_0^\infty C(t)dte^{i\omega t}, \tag{20}$$

and proceeding in the same way as in Eq. (14),

$$D(\Delta\omega)=-\frac{1}{\pi}\int_0^\infty[\cos(\Delta\omega t)C_I(t)+\sin(\Delta\omega t)C_R(t)]. \tag{21}$$

D. Line profiles of polarization signals

As we have mentioned before, the profile recorded with polarization spectroscopy results in the sum of the squares of the absorption and the dispersion profiles:

$$P(\Delta\omega)=A(\Delta\omega)^2+D(\Delta\omega)^2. \tag{22}$$

$P(\Delta\omega)$ is, therefore, the square of the module of the Fourier transform of $C(t)$. Since $C(t)$ is real, $P(\Delta\omega)$ can be put as the cosine transform of the autocorrelation function of $C(t)$:

$$P(\Delta\omega)=\frac{2}{\pi}\int_0^\infty dt\,\cos(\Delta\omega t)\int_0^\infty d\tau C(\tau)C(\tau+t). \tag{23}$$

In a calculation by computer simulation, the normalization of the spectral absorption profiles is obtained establishing $C(t=0)=1$. In the case of a polarization spectrum, the condition

$$\int_{-\infty}^{+\infty}P(\Delta\omega)d\Delta\omega=1 \tag{24}$$

requires that

$$2\int_0^\infty dtC(t)^2=1. \tag{25}$$

IV. MATHEMATICAL TREATMENT OF THE SIMULATION

The physical plasma model adopted in this work as well as the simulation method are identical to that used in Ref. [5]. In this section we will summarize briefly the fundamental ideas of the simulation process and give an account of the specific parameters in this work. The main difference between the mathematical treatment in the simulation in this work and in the previously mentioned one is about the emitter atom, but not in what refers to the ensemble of perturbers.

A. Plasma model

We consider a weakly coupled, homogeneous and isotropic plasma where the particles are independent and move along rectilinear paths with constant velocity. Those velocities satisfy a Maxwell-Boltzmann distribution according to the μ-ion model [3]. In the simulation a finite spherical volume is assumed with N_P ions and N_P electrons. The emitter

is placed at the center of the sphere. The method of substituting the particles that reach the edge of the sphere, which is the most delicate aspect of the simulation technique, is detailed in Ref. [5]. This method guarantees that the statistical distributions used (homogeneity and isotropy of the particles' positions, isotropy of the paths, and Maxwellian distribution for the velocity) are steady with the time [22] and that there is no correlation between the outgoing particles and the incoming ones.

Table I summarizes the number of considered particles in the different simulation processes. Those numbers of particles are enough to guarantee the quality of the results since the nearest particles are the ones that completely determine the mean behavior of the autocorrelation function of the dipole moment of the emitter [5].

The electric field of the ensemble of simulated ions and electrons is evaluated at the center of the sphere according to the expression of the Debye shielded field in order to take into account, at least in an approximate way, the correlation effects between charged particles of different sign.

As is mentioned in Ref. [5], we have used the same numerical sequence of the electric microfield to study several cases of density and temperature mutually bound through the parameter $\rho = R_0/R_D$, that characterizes the dimensions of a numerical simulation process. In that expression $R_0 = [3/(4\pi N_e)]^{1/3}$ is the mean interparticle distance—N_e is the electronic density—and $R_D = \sqrt{\epsilon_0 kT/q_e^2 N_e}$ is the Debye radius of the system at the temperature T. The high number of temporary sequences employed in the simulations allows us to work without any mechanism of sample selection; in particular, the control over the initial conditions of each simulation, as is already done in Ref. [5].

Once the temporary microfield sequence is established, it is used by the differential equations (8) that set up the evolution of the dipole moment of the emitter atom. These equations have been solved considering the microfield sequence as a stepped function in which the electric field is constant in the interval between two temporary steps. The step size used (in our case $\Delta\tau = 0.01 R_0/v_{0e}$ with v_{0e} the mean square speed of the electrons) allows us to guarantee the quality of the numerical integration [22]. In this way, in each temporary step τ_j of the process of simulation the evolution operator is

$$\begin{aligned} U(\tau_j) &= U(\tau_{j-1}+\Delta\tau, \tau_{j-1})U(\tau_{j-1}), \quad U(0) = \mathbb{1} \\ U(\tau+\Delta\tau, \tau) &= \exp\left[-\frac{i}{\hbar}H(\tau)\Delta\tau\right] \\ &= \sum_k \exp\left[-\frac{i}{\hbar}H_k(\tau)\Delta\tau\right]P_k(\tau), \end{aligned} \tag{2.6}$$

where $H(\tau) = H_0 + q\mathbf{E}(\tau)\cdot\mathbf{R}$ is the Hamiltonian of the emitter at the instant τ and $P_k(\tau)$ is the projector on the subspace of eigenstates of $H(\tau)$ with eigenvalue $H_k(\tau)$.

B. Emitter atom model

1. Calculation of the evolution operator

The Lyman-α line is produced in a transition between the states $n=2$ and $n=1$ in the hydrogen atom. The lower level has two degenerated states that, in *no-quenching* approximation, are not altered by the presence of an external electric field. In the absence of a perturber electric field, the states of the upper level have an energy that depends on the quantum number j [23]. In the case $n=2$, the values of j are $\frac{1}{2}$ and $\frac{3}{2}$, so that the eigenvalues of H_0 are $\pm s = \pm 3.6227\times10^{-24}$ J $= \pm 2.2613\times10^{-5}$ eV, where we have taken the ''center of gravity'' of the group of states as the origin of energies. In the presence of an external electric field **E**, the Hamiltonian of the upper level takes the form [23]

$$H = \begin{pmatrix} -s & 0 & -\sqrt{\frac{1}{3}}F_0 & -\sqrt{\frac{2}{3}}F_+ & -F_- & -\sqrt{\frac{2}{3}}F_0 & -\sqrt{\frac{1}{3}}F_+ & 0 \\ 0 & -s & \sqrt{\frac{2}{3}}F_- & \sqrt{\frac{1}{3}}F_0 & 0 & -\sqrt{\frac{1}{3}}F_- & -\sqrt{\frac{2}{3}}F_0 & -F_+ \\ -\sqrt{\frac{1}{3}}F_0 & -\sqrt{\frac{2}{3}}F_+ & -s & 0 & 0 & 0 & 0 & 0 \\ \sqrt{\frac{2}{3}}F_- & \sqrt{\frac{1}{3}}F_0 & 0 & -s & 0 & 0 & 0 & 0 \\ F_+ & 0 & 0 & 0 & s & 0 & 0 & 0 \\ -\sqrt{\frac{2}{3}}F_0 & \sqrt{\frac{1}{3}}F_+ & 0 & 0 & 0 & s & 0 & 0 \\ \sqrt{\frac{1}{3}}F_- & -\sqrt{\frac{2}{3}}F_0 & 0 & 0 & 0 & 0 & s & 0 \\ 0 & F_- & 0 & 0 & 0 & 0 & 0 & s \end{pmatrix}, \tag{27}$$

TABLE I. Working conditions of the simulations: N_p, number of electrons; $\log_{10} N_e$, range of the electronics densities simulated in m^{-3}, with increments of $\frac{1}{3}$ of decade.

ρ	N_p	Samples	$\log_{10} N_e$
0.10	250	6128	19.66–21.33
0.15	250	9106	19.66–22.00
0.20	250	14645	19.66–22.33
0.25	200	12564	19.66–23.00
0.30	175	12177	20.00–23.00
0.40	100	11234	20.66–23.00
0.50	100	10708	21.00–23.00
0.60	100	12593	21.00–23.00
0.70	100	12817	22.00–23.00

where $F_0 \equiv 3qa_0E_z$ and $F_\pm \equiv \mp 3qa_0(E_x \pm iE_y)/\sqrt{2}$. The selected base of states is $|j,l,m_j\rangle$ with $j=\{1/2(l=0),1/2(l=1),3/2(l=1)\}$, $m_j=\{-j,\ldots,+j\}$. The presence of the electric field partially breaks the degeneracy in m_j. The eigenvalue equation of the matrix H is

$$(H-s_1)\left[H^3+sH^2-(s^2+F^2)H-\left(s^3+\frac{1}{3}sF^2\right)\mathbb{1}\right]=0. \tag{28}$$

One of the eigenvalues is independent of the electric field. In order to obtain the other three eigenvalues, we define the matrix

$$M \equiv \frac{1}{f}\left(H+\frac{1}{3}s\right) \tag{29}$$

(f is a quantity that will be determined later) so that the eigenvalues that depend on the field **F** are obtained from the polynomial

$$f^3M^3-\left(\frac{4}{3}s^2+F^2\right)fM-\frac{16}{27}s^3\mathbb{1}=0. \tag{30}$$

We make

$$f \equiv \frac{4}{3}s\sqrt{1+\left(\frac{\sqrt{3}F}{2s}\right)^2}=\frac{4s}{3\cos\varphi}, \tag{31}$$

$$\tan\varphi \equiv \frac{\sqrt{3}F}{2s}, \tag{32}$$

then Eq. (30) can be rewritten as

$$4M^3-3M=\cos^3\varphi. \tag{33}$$

The latter is the Chebyshev polynomial [24] $T_3(M)$ corresponding to the expansion $\cos(3\theta)=4\cos^3(\theta)-3\cos(\theta)$, so that the solutions of Eq. (33) can be written as

$$M_k=\cos(\theta_k),$$
$$\theta_k=\frac{1}{3}\arccos[\cos^3\varphi]+\frac{2k\pi}{3}, \quad k=0,1,2. \tag{34}$$

The eigenvalues of H are then (see Fig. 1)

$$H_k=\frac{s}{3}\left(\frac{4\cos\theta_k}{\cos\varphi}-1\right), \quad k=0,1,2$$
$$H_3=s. \tag{35}$$

The calculation of the eigenstates of H is straightforward: the projectors P_k on each one of the spaces of the states with eigenvalue H_k can be obtained analytically through the expression

$$P_k=\frac{\prod_{j\neq k}(H-H_k\mathbb{1})}{\prod_{j\neq k}(H_j-H_k)}. \tag{36}$$

In the numerical calculation, these formulations, when inserted into the relationship (26), allow us to obtain the sequence of the evolution operator of the upper level. The group of lower states is not affected by the collisions of the perturbers, so that in expression (11) we can set $U_l=\mathbb{1}$.

2. Calculation of the autocorrelation function

The transition studied in this work connects the lower state $1S$ with the upper state $2S$. This jump is obtained by the absorption of two photons without an intermediate atomic level. The absorption of the first photon puts the atom in a state in which it is maintained about 1 fs [10]. In that interval the absorption of the second photon must be produced. In the scale of characteristic times of loss of correlation, both photons are absorbed simultaneously so that in the transition process no change is produced in the phase of the evolution operator. This allows us to establish as a jump operator that plays the role of the dipole operator **d** in Eq. (7) the matrix that connects the states $1S$ of the lower level with the $2S$ of the upper level. It must be taken into account that in that transition $\Delta l=0$ must be satisfied. In the base of states that we are using, such a normalized transition matrix takes the form

$$d^\dagger=\frac{1}{\sqrt{2}}\begin{pmatrix}1&0&0&0&0&0&0&0\\0&1&0&0&0&0&0&0\end{pmatrix}. \tag{37}$$

In this way, the autocorrelation function describes the evolution of the level $2S$.

C. Simple model of static ions

If we do not take into account the dynamical effects of the collisions of ions and electrons with the emitter atom, that is to say, if we consider that the electric field **E** in Eq. (8) is constant in time, then the solution of the differential equations leads to

$$U(t)=\exp\left[-\frac{i}{\hbar}Ht\right]=\sum_{k=0}^{3}e^{-(i/\hbar)H_kt}P_k, \tag{38}$$

where the eigenvalues H_k and the projectors P_k depend on the static electric field **E** of the configuration. Substituting this expression into Eq. (10) we obtain

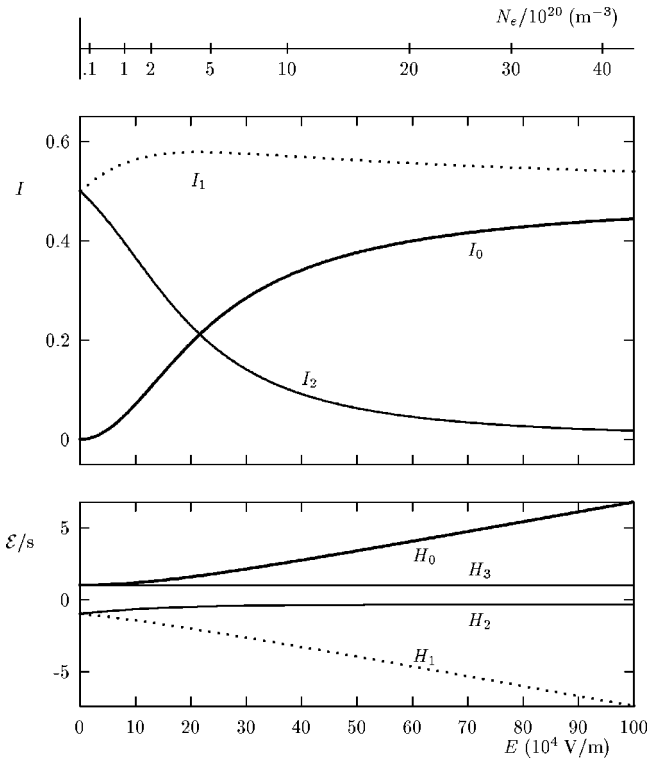

FIG. 1. Middle figure: Relative intensity, $I_i = \mathrm{tr}(dd^\dagger \mathcal{P}_i)$, of the corresponding transitions of the two-photon absorption process between the levels $n=1$ and $n=2$ in the hydrogen atom as a function of the applied static electric field. Lower figure: Eigenvalues H_i (in units of the separation s of fine structure) of the level $n=2$ as a function of the applied electric field. The subscripts 0, 1, and 2 of these figures correspond to those of the components that depart from the levels 0, 1, and 2, in accordance with the notation employed in Eq. (35). The upper scale represents the perturber density that would have as typical field the field E of the X axis.

$$C(t) = 2\ \mathrm{Re} \sum_{k=0}^{3} \exp\left[-i\left(\omega_0 + \frac{1}{\hbar} H_k \right) t \right] \mathrm{tr}(dd^\dagger P_k). \tag{39}$$

Carrying out operations in Eq. (36), it is found that, for the absorption spectrum of two photons (see Fig. 1),

$$\mathrm{tr}(dd^\dagger P_k) = \frac{2}{3} \frac{[\cos(\theta_k) - \cos(\varphi)][2\cos(\theta_k) + \cos(\varphi)]}{4\cos^2(\theta_k) - 1}, \tag{40}$$

$$k = 0,1,2,$$

$$\mathrm{tr}(dd^\dagger P_3) = 0.$$

The broadening effect of the quick collisions due to the electrons can be taken into account following an impact model [16] replacing the real eigenvalues H_k with the quantities $H_k - i\Phi_k$ so that the spectrum corresponding to the configuration of static electric field $\mathbf{E}$ is

$$A(\Delta\omega, \mathbf{E}) = \frac{1}{\pi}\ \mathrm{Re} \sum_k \frac{1}{i(H_k - \hbar\Delta\omega) + \Phi_k}\ \mathrm{tr}(dd^\dagger P_k). \tag{41}$$

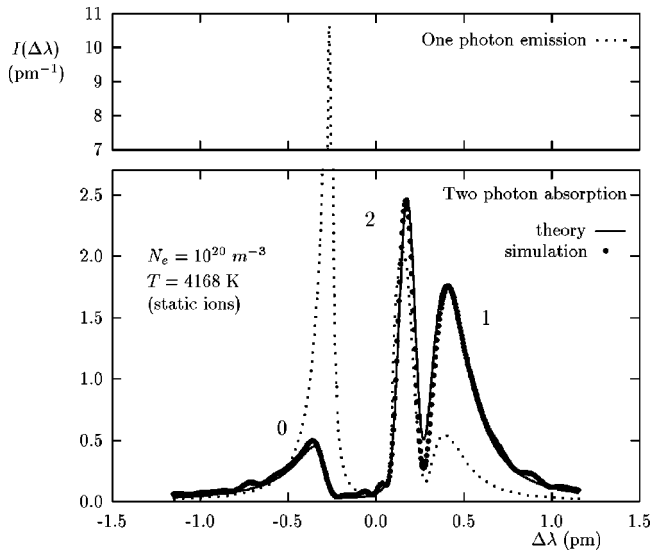

FIG. 2. Two-photon absorption spectrum ($1S \rightarrow 2S$) according to a quasistatic broadening model for the ionic collisions and an impact model for the electronic collisions. In this figure we show the dipole one-photon emission profile of the transition $n=2 \rightarrow n=1$. Both profiles are area normalized. The labels 0, 1, and 2 of this figure correspond to those of the components that depart from the levels 0, 1, and 2, in accordance with the notation employed in Eq. (35).

Then the total spectral profile is obtained averaging this function on all the possible configurations of static field

$$A(\Delta\omega) = \int d^3\mathbf{E} W(\mathbf{E}) A(\Delta\omega, \mathbf{E}), \tag{42}$$

where $W(\mathbf{E})$ is the statistical distribution of the static field [25].

The result of an analytical calculation, according to the previous expressions, of the two-photon absorption spectrum in the transition studied is shown in Fig. 2, in comparison with a simulation accomplished with static ions. In the analytical calculation $\Phi_0 = \Phi_2 = 0.013$ pm and $\Phi_1 = 0.020$ pm. Figure 2 also shows the dipole emission Lyman-α spectrum obtained in the simulation with static ions, under the same conditions of electronic density and temperature, to show the relative situation of both types of profiles.

In Fig. 3 we show a sequence of polarization profiles by two-photon absorption obtained by computer simulation with practically static ions ($\mu = 1000$ in units of the mass of the proton). It can be seen how the shape of the profiles is modified with the density due to two reasons: First, due to the change in the width of the components, and, second, by the dependency of the transition probabilities with the intensity of the typical static field that gives rise to the Stark effect (see Fig. 1).

V. RESULTS

Table I summarizes the specific cases of ρ and density of the plasma considered in this work. In each one of those conditions, the calculation is carried out with values of the parameter $\mu = 0.5$, 1.0, and 2.0, that covers the cases of experimental interest, and in some ($\rho = 0.3$–0.7), furthermore,

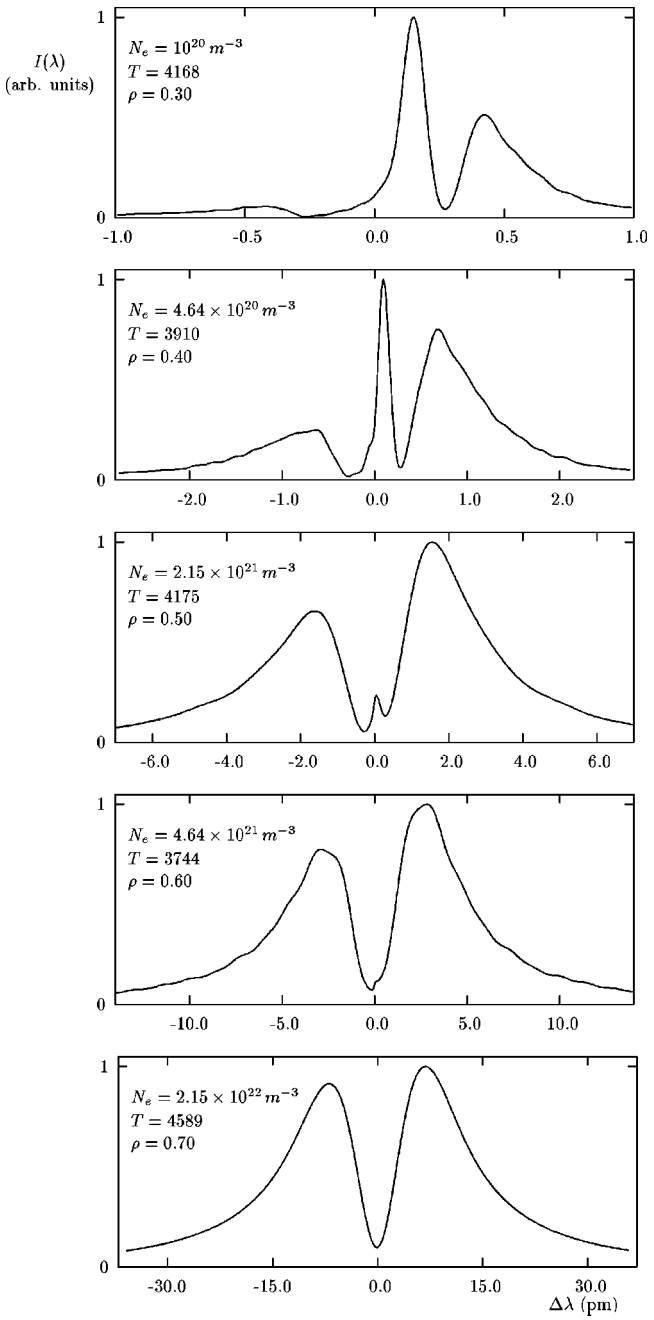

FIG. 3. Sequence of polarization profiles obtained in the simulation for different values of the density and of the parameter ρ of the plasma. In all cases, $\mu = 1000$, that is to say, nearly static ions.

for $\mu = 5.0$, 10.0, 50.0, 100.0, and 1000.0, in order to study the extrapolation to static ions. Also we have calculated the special cases of density and temperature of the experimental data shown below in the comparison of theory and experience.

In Fig. 4 we show the behavior of the FWHM of the polarization spectra with the electronic density. As density decreases, the width presents an almost linear response with the density, as is characteristic of the impact broadening. In this range, the loss of coherence in the emission process due to the individual collisions is very small, so that even the ionic collisions are in the impact dominance (see Ref. [5] for discussion of this aspect). At high densities, the width tends to follow a behavior as $N_e^{2/3}$, that reflects the influence of the

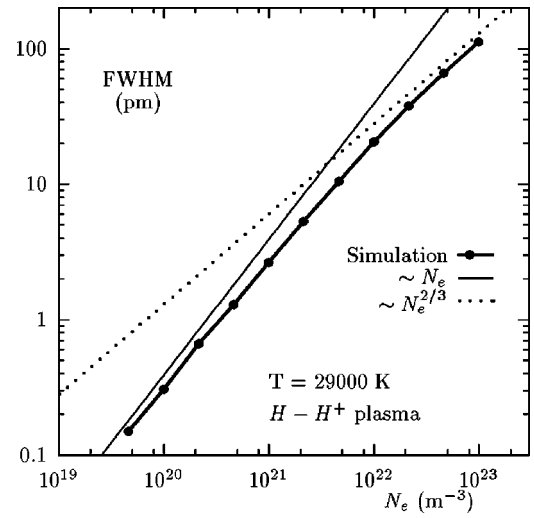

FIG. 4. Full width at half maximum of the polarization profiles at constant temperature obtained in the simulation as a function of the electronic density. In this case, $\mu = 0.5$.

quasistatic part of the broadening mechanisms.

The influence of the temperature and the mass of the perturbers is summarized in Fig. 5. At low densities we are in the impact broadening domain—even for the ions—that is rendered in a behavior of the width of the line with the temperature in the form $T^{-1/2}$. That is to say, the quicker the emitter-perturber collisions are, the smaller their effects on

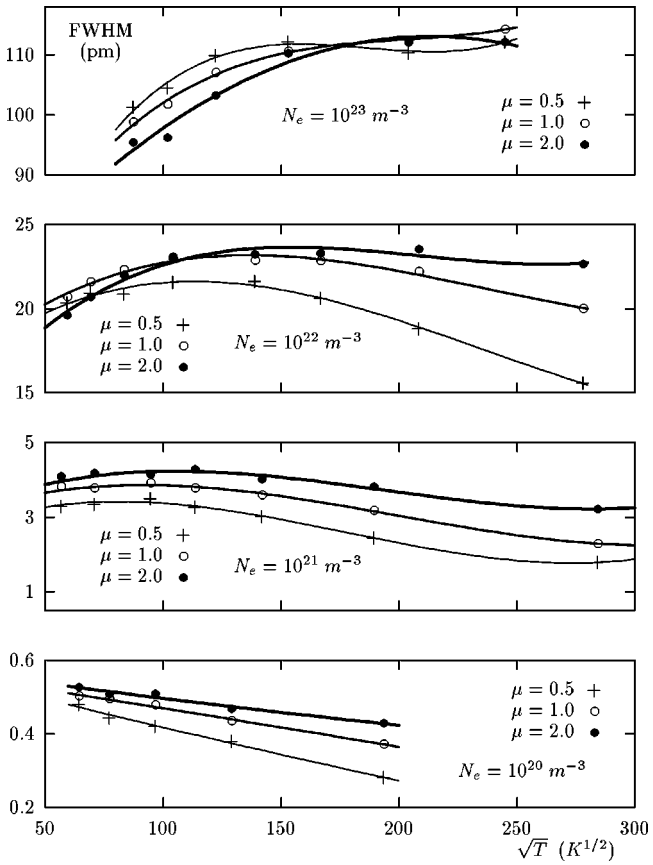

FIG. 5. Full width at half maximum of the polarization profiles obtained in the simulation as a function of the temperature for several conditions of electronic density and mass of the perturbers.

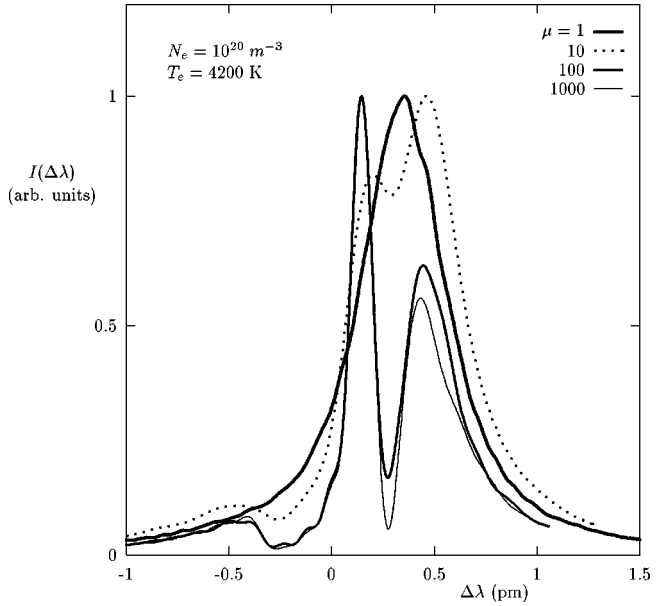

FIG. 6. Polarization profiles obtained in the simulation for different conditions of the mass of the perturbers. The spectra are normalized in height.

the coherence loss are. Then, in that regime, the bigger the perturber mass is, the slower their movement is, and as a consequence their collisions with the emitter are more effective, that implies a larger width. In the other extreme, at high densities, we are in the domain of the quasistatic effects of the ionic collisions, so that the trend with the temperature and the mass of the perturbers is reversed. In this case, the effects of ion dynamics tend to increase the width of the lines, which gives rise to an increase of the width as the reduced mass of the emitter-perturber pair decreases. In the intermediate zone is produced the transition between those two domains that we have considered, on one hand, of dynamical broadening of the ions (that increases with the temperature) and, on the other hand, of ionic impact broadening (that decreases with the temperature).

In Fig. 6 we show the result of an academic calculation of the polarization profile with growing values of the reduced

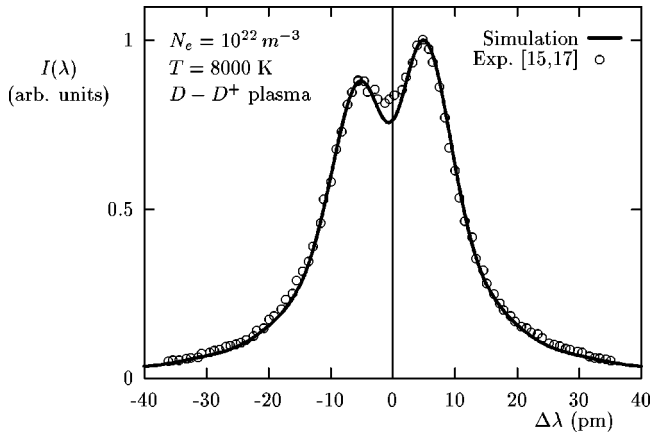

FIG. 7. Comparison between experimental data [12,14] (D-D^+ plasma) and the results of the simulation. The conditions of this plasma were obtained from Balmer profiles registered in the same experiment [12].

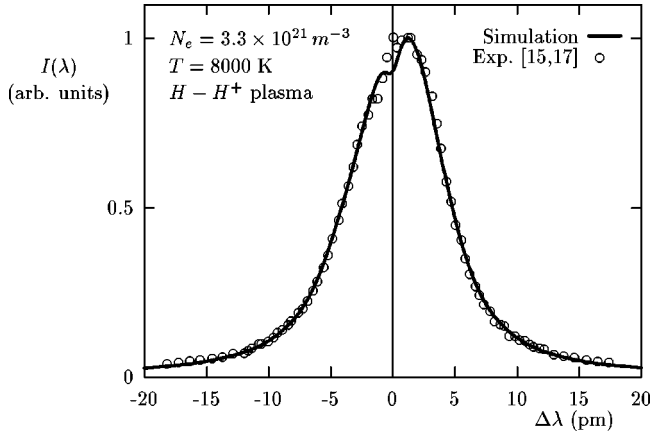

FIG. 8. Comparison between experimental data [12,14] (H-H^+ plasma) and the results of the simulation.

mass μ of the emitter-perturber pair. The most important effect due to the change of the perturber mass is the drastic change of the shape of the spectral profile. The effects of ion dynamics in this spectral line are fundamental. Though this result seems impossible to confirm experimentally (the realistic values of μ in the plasmas in equilibrium are between 0.5 and 2) in plasmas out of equilibrium, where the emitter and the ionic perturbers are at a much lower temperature than the electrons, the configuration can be equivalent to that of ions and the static emitter surrounded by a cloud of electrons of great mobility. In those cases, the calculations by computer simulation can be useful in order to make plasma diagnosis tables.

The calculations that are presented include the fine structure of the level $n=2$, of course. This is indispensable for low densities, since the level structure completely marks the shape of the profiles. But even at high densities, the effect of the fine structure on the shape of the profile (though no longer in the width) is still appreciated: the spectra are asymmetrical as a consequence of the relationship of the intensities of the components [14], especially of the two lateral components (those that in Fig. 2 are labeled with 0 and 1)

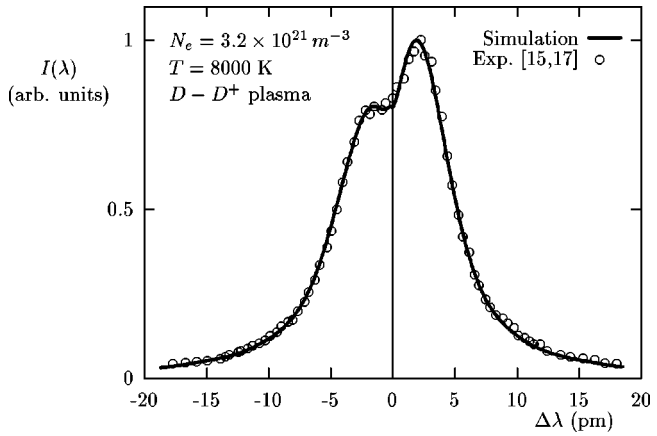

FIG. 9. Comparison between experimental data [12,14] (D-D^+ plasma) and the results of the simulation. The conditions of this plasma were obtained from Balmer profiles registered in the same experiment [12].

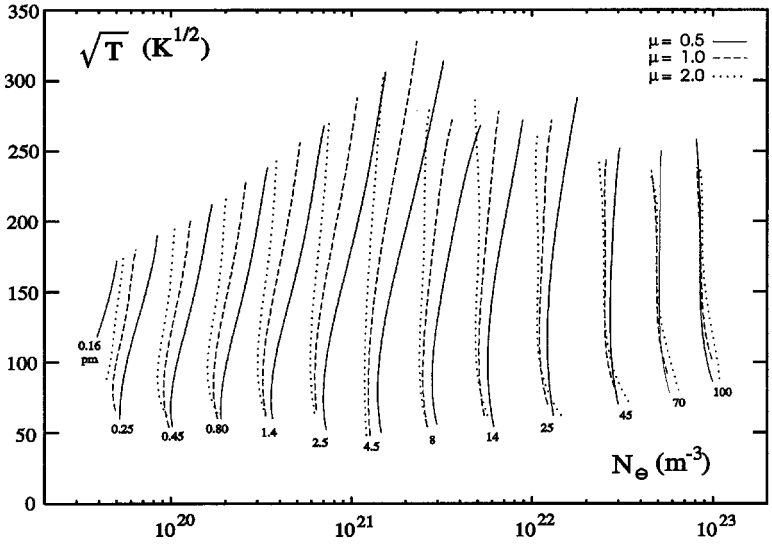

FIG. 10. Full width at half maximum curves of the two-photon absorption polarization spectrum in the transition $1S \rightarrow 2S$ of the hydrogen. The curves represent a constant value of the width (in pm) as a function of the electronic density and temperature. The curves corresponding to three different values of the mass μ of the ionic perturbers have been represented.

that tend to have the same intensity for very high electric fields (see Fig. 1).

A. Comparison with experimental data

The only experiments that we know of on polarization spectroscopy by two-photon absorption in the Lyman-alpha transition are documented in Refs. [9–11, 13, 14] and, especially, in Ref. [12]. In this last experiment a continuous arch stabilized at low pressure with pure hydrogen (plasma with $\mu = 0.5$) and pure deuterium ($\mu = 1.0$) was employed. The diagnosis of the plasma was carried out through the record of the Stark broadened spectra of the Balmer-β and Balmer-γ lines.

We have reproduced those Balmer profiles by computer simulation [5] in order to determine the electronic density. The same plasma conditions were fixed for the Balmer-β and Balmer-γ lines and for the polarization profiles. The results are shown in Figs. 7–9. In all cases we have employed the Balmer lines to determine the electronic density that should be used in the simulation calculations. An excellent agreement between calculation and experiment can be seen in all the cases compared.

B. Conclusions

The calculation method used in this work for obtaining polarization spectra is sufficiently effective and it can be employed to make spectrum tables that can be used in plasma diagnosis. In the specific case studied here, the transition Lyman-α by two-photon absorption, the relationship between the width of the spectral line and the electronic density can serve as a diagnostic method of sufficient quality. The influence of the temperature on the shape of the profiles is smaller than the influence of charged perturber density, so that the determination of the electronic density through the measurement of the FWHM of the spectra can be carried out with great precision. Figures 10 and 11 show maps of constant FWHM in the spectra that are obtained through polarization spectroscopy by two-photon absorption techniques in a wide range of electronic densities and temperatures. In Fig. 10 the influence of the mass of the perturbers on the spectral width can be clearly seen. Figure 11, where our results for the case of a pure hydrogen plasma are summarized, is of practical use for diagnosis. The measure of the FWHM of the studied spectrum allows us to set bounds to the values of the electronic density and temperature of the plasma.

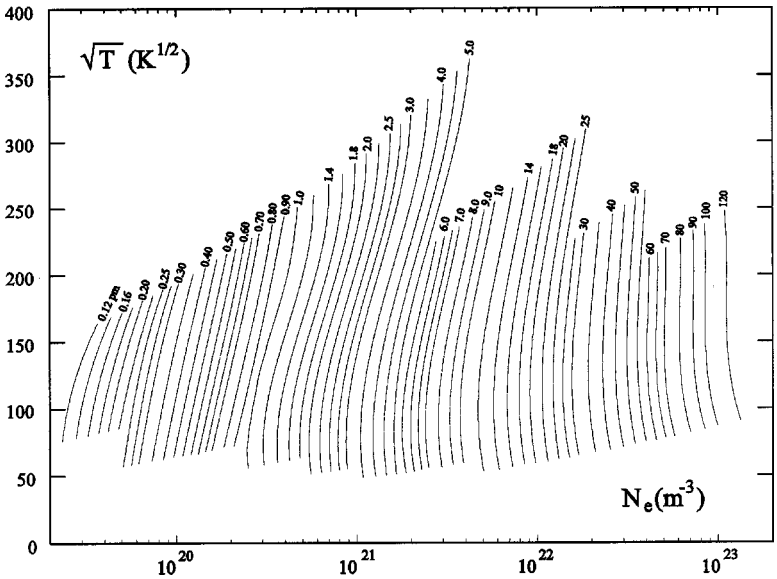

FIG. 11. Full width at half maximum curves of the two-photon absorption polarization spectrum in the transition $1S \rightarrow 2S$ of the hydrogen. The curves represent a constant value of the width (in pm) as a function of the electronic density and temperature. In this case, $\mu = 0.5 m_p$ (m_p is the mass of the proton), that corresponds to the case of a pure hydrogen plasma.

ACKNOWLEDGMENTS

The authors of this work wish to thank Dr. Klaus Grützmacher for his valuable suggestions. This work has been financed by the Universidad de Valladolid and, partially, by the DGICYT (Project No. PB94-0216). Most of the means of calculation belong to the Departamento de Informática of the Universidad de Valladolid. We want to thank Professor Valentín Cardeñoso for his close collaboration in the development of the work and Professor González Vizmanos and Professor Fuentes García for their help in the maintenance of the calculations.

[1] D. E. Kelleher, W. L. Wiese, V. Helbig, R. L. Greene, and D. H. Oza, Phys. Scr. **T47**, 75 (1993).
[2] D. H. Oza, R. L. Greene, and D. E. Kelleher, Phys. Rev. A **38**, 2544 (1988).
[3] J. Seidel and R. Stamm, J. Quant. Spectrosc. Radiat. Transf. **27**, 499 (1982).
[4] M. A. Gigosos, V. Cardeñoso, and F. Torres, J. Phys. B **19**, 3027 (1986).
[5] M. A. Gigosos and V. Cardeñoso, J. Phys. B **29**, 4795 (1996).
[6] V. Cardeñoso and M. A. Gigosos, J. Phys. B **30**, 3361 (1997).
[7] T. W. Hänsch, S. A. Lee, R. Wallenstein, and C. Wieman, Phys. Rev. Lett. **34**, 307 (1975).
[8] P. F. Liao and G. C. Bjorklund, Phys. Rev. Lett. **36**, 584 (1976).
[9] K. Danzmann, K. Grützmacher, and B. Wende, Phys. Rev. Lett. **57**, 2151 (1986).
[10] J. Seidel, Phys. Rev. Lett. **57**, 2154 (1986).
[11] K. Grützmacher and A. Steiger, in *9th International Conference of Spectral Line Shapes (ICSLS), Toruń, Poland, 1988*, edited by J. Szudy (Ossolineum, Wrocław, 1989), p. 35.
[12] A. Steiger, Ph.D. dissertation, Technische Universität Berlin, 1993.
[13] A. Steiger and K. Grützmacher, in *11th International Conference of Spectral Line Shapes (ICSLS), Carry le Rouet, France, 1992*, edited by R. Stamm and B. Talin (Nova Science, New York, 1993), p. 141.
[14] J. Seidel, A. Steiger, and K. Grützmacher, in *12th International Conference of Spectral Line Shapes (ICSLS), Toronto, Canada, 1994*, edited by A. David May, J. R. Drummond, and E. Oks (AIP Press, New York, 1995), p. 32.
[15] W. Demtröder, *Laser Spectroscopy* (Springer, Berlin, 1996).
[16] H. R. Griem, *Spectral Line Broadening by Plasmas* (Academic Press, New York, 1974).
[17] E. U. Condon and G. H. Sortley, *The Theory of Atomic Spectra* (Cambridge University Press, London, 1967).
[18] I. I. Sobel'man, L. A. Vainshtein, and E. A. Yukov, *Excitation of Atoms and Broadening of Spectral Lines* (Springer-Verlag, Berlin, 1981).
[19] K. A. Berington *et al.*, J. Phys. B **20**, 6379 (1987).
[20] J. D. Jackson, *Classical Electrodynamics* (John Wiley, New York, 1975).
[21] L. Schwartz, *Mèthodes Mathèmatiques pour les Sciences Physiques* (Hermann, Paris, 1965), p. 46.
[22] M. A. Gigosos and V. Cardeñoso, J. Phys. B **20**, 6006 (1987).
[23] H. A. Bethe and E. E. Salpeter, *Quantum Mechanics of One- and Two-Electron Atoms* (Springer-Verlag, Berlin, 1957).
[24] *Handbook of Mathematical Functions*, edited by M. Abramowitz and A. Stegun (Dover, New York, 1972).
[25] C. F. Hooper, Jr., Phys. Rev. **169**, 193 (1968).